

1 ***De novo* disease-associated mutations in KIF1A dominant negatively inhibit axonal transport**
2 **of synaptic vesicle precursors**

3

4 Yuzu Anazawa^{1,4}, Tomoki Kita^{2,4}, Kumiko Hayashi² and Shinsuke Niwa^{1,3,#}

5

6

7

8 ¹Graduate school of Life Sciences, Tohoku University, Katahira 2-1, Aoba-ku, Sendai, Miyagi
9 980-8578, Japan

10 ²Department of Applied Physics, Graduate school of Engineering, Tohoku University, Aramaki-Aoba
11 6-6-05, Aoba-ku, Sendai, Miyagi, Japan

12 ³Frontier Research Institute for Interdisciplinary Sciences (FRIS), Tohoku University, Aramaki-Aoba
13 6-3, Aoba-ku, Sendai, Miyagi 980-0845, Japan

14 ⁴These authors contributed equally to this work

15

16 #Corresponding author:

17 SHINSUKE NIWA, Frontier Research Institute for Interdisciplinary Sciences (FRIS), Tohoku
18 University, Aramaki-Aoba 6-3, Aoba-ku, Sendai, Miyagi 980-0845, Japan

19 e-mail: shinsuke.niwa.c8@tohoku.ac.jp

20

21

22

23

24

25 **Abstract**

26 KIF1A is a kinesin superfamily molecular motor that transports synaptic vesicle precursors in axons.
27 Mutations in *Kif1a* lead to a group of neuronal diseases called KIF1A-associated neuronal disorder
28 (KAND). KIF1A forms a homodimer and KAND mutations are mostly *de novo* and autosomal
29 dominant; however, it is not known whether the function of wild-type KIF1A is inhibited by
30 disease-associated KIF1A. No reliable *in vivo* model systems to analyze the molecular and cellular
31 biology of KAND have been developed; therefore, here, we established *Caenorhabditis elegans*
32 models for KAND using CRISPR/cas9 technology and analyzed defects in axonal transport. In the *C.*
33 *elegans* models, heterozygotes and homozygotes exhibited reduced axonal transport phenotypes. In
34 addition, we developed *in vitro* assays to analyze the motility of single heterodimers composed of
35 wild-type KIF1A and disease-associated KIF1A. Disease-associated KIF1A significantly inhibited
36 the motility of wild-type KIF1A when heterodimers were formed. These data indicate the molecular
37 mechanism underlying the dominant nature of *de novo* KAND mutations.

38

39 **Keywords:** axonal transport, KAND, neuropathy, kinesin, UNC-104, KIF1A

40

41

42

43

44

45

46

47

48

49 **Significance Statement**

50 KIF1A is a molecular motor that transports synaptic vesicle precursors in axons. Recent studies have
51 identified many *KIF1A* mutations in congenital neuropathy patients; however, the molecular
52 mechanism of pathogenesis remains elusive. This study established a model for KIF1A-associated
53 neuronal disorder (KAND) in *Caenorhabditis elegans* to analyze the molecular and cell biology of
54 the disease *in vivo*. This study also established *in vitro* single-molecule assays to quantitatively
55 analyze the effect of KAND mutations when mutant KIF1A forms heterodimers with wild-type
56 KIF1A. Our findings provide a foundation for future genetic screening and for drug screening to
57 search for KAND treatments.

58

59

60

61

62

63

64

65

66

67

68

69

70

71

72

73 **Introduction**

74 Neuronal function depends on specific intracellular transport called axonal transport (1-3).
75 Neurons transmit information via synaptic vesicles that accumulate at synapses (4). The constituents
76 of synaptic vesicles are synthesized and assembled in the cell body and transported down axons to
77 synapses. The transported organelle is called a synaptic vesicle precursor (5). KIF1A is a kinesin
78 superfamily protein that transports synaptic vesicle precursors in axons (5, 6). KIF1A has a motor
79 domain and a cargo-binding tail domain (5). The motor domain, which is conserved among Kinesin
80 superfamily members, has microtubule-dependent ATPase activity that drives movement on
81 microtubules (7, 8). The tail domain of KIF1A is composed of a protein-binding stalk domain and a
82 lipid binding Pleckstrin-homology (PH) domain (6, 9-11).

83 *Caenorhabditis elegans* (*C. elegans*) is a good model animal to study axonal transport
84 (12-19). UNC-104 is a *C. elegans* orthologue of KIF1A (20, 21). Electron and light microscopy
85 analyses have shown that synapses as well as synaptic vesicles are mislocalized in *unc-104* mutants
86 (20). The mechanism of axonal transport is well conserved between *C. elegans* and mammals and
87 the expression of a human *Kif1a* cDNA can rescue the phenotype of *unc-104* mutant worms (22).

88 Mutations in the motor domain of *KIF1A* can cause congenital neuropathies (23, 24). More
89 than 60 mutations have been found in the motor domain of *KIF1A* in neuropathy patients. Some
90 cases are familial, but most are sporadic. For example, KIF1A(R11Q) was found in autism spectrum
91 disorder and attention-deficit hyperactivity disorder (25), and KIF1A(R254Q) was found in Japanese
92 spastic paraplegia patients (26). KIF1A(R254) is a hot spot for a broad range of neuropathies, such
93 as KIF1A(R254W), have been described in non-Japanese patients (24). These neuropathies caused
94 by KIF1A mutations is called KIF1A-associated neuronal disorder (KAND). Both dominant and
95 recessive mutations are associated with KAND. KAND is caused by both gain of function and loss
96 of function mechanisms. We have shown that familial mutations, KIF1A(V8M), KIF1A(A255V) and

97 KIF1A(R350G), over activate KIF1A and axonal transport. Recent *in vitro* studies have shown that
98 *de novo* KAND mutations are loss of function. KIF1A(P305L) reduces the microtubule association
99 rate of the motor (27). KIF1A(R169T) disrupts the microtubule-dependent ATPase activity of the
100 motor domain (28). KIF1A(R254W) reduces the velocity and run length of the motor protein (24) .

101 While these loss of function mutations have been intensively studied using *in vitro* assays,
102 reliable models to study the neuronal cell biology of KAND mutations *in vivo* are awaited. Moreover,
103 previous *in vitro* studies have mostly analyzed homodimers composed of disease-associated KIF1A
104 (24, 27) because it was difficult to purify heterodimers composed of wild-type and
105 disease-associated KIF1A (29). Activated KIF1A forms a homodimer to move on microtubules (30);
106 therefore, wild-type KIF1A is very likely to dimerize with disease-associated KIF1A in patient
107 neurons. However, it is not known whether *de novo* KAND mutations inhibit the function of
108 wild-type KIF1A in a dominant negative fashion.

109 Here, we established *C. elegans* models of *de novo* KAND mutations. Heterozygous
110 worms, as well as homozygous worms, show synaptic deficiencies that are caused by axonal
111 transport defects. We also established an *in vitro* single molecule analysis system to measure the
112 motility parameters of a single heterodimer composed of wild-type and disease-associated KIF1A.
113 Heterodimers composed of wild-type KIF1A and disease-associated KIF1A showed reduced motility
114 *in vitro*.

115

116 **Results**

117 ***C. elegans* models of *de novo* KAND**

118 To study molecular and cellular deficiencies caused by *de novo* disease-associated KIF1A mutations,
119 we established *C. elegans* models for KAND using CRISPR/cas9 (31). *C.elegans unc-104* gene is an
120 orthologue of human *Kif1a*. We introduced following mutations in *unc-104* gene: *unc-104(R9Q)*,

121 *unc-104(R251Q)* and *unc-104(P298L)* (Figure 1A and B). These *unc-104* residues are conserved in
122 human KIF1A and these mutations correspond to KIF1A(R11Q), KIF1A(R254Q) and
123 KIF1A(P305L) mutations, respectively. All of them are causes of *de novo* and autosomal dominant
124 KAND (25-27). Introduction of mutations was confirmed by Sanger sequencing. Then, we observed
125 the macroscopic phenotypes of disease model worms. The body size of homozygous worms was
126 smaller than that of wild-type worms [1.09 ± 0.09 mm, 0.66 ± 0.06 mm, 0.64 ± 0.07 mm, $0.74 \pm$
127 0.06 mm, respectively for *wild type*, *unc-104(R9Q)*, *unc-104(R241Q)*, and *unc-104(P298L)*] (Figure
128 1C). Moreover, homozygous worms showed uncoordinated (*unc*) phenotypes and did not move well
129 on the culture plate (Figure 1C). To quantitatively analyze the movement of worms, the number of
130 body bends in a water drop was counted during one minute (Figure 1D). We found homozygous
131 worms did not move well in the water. These results collectively show that all three mutants
132 phenocopy a well-established loss-of-function allele of *unc-104*, such as *unc-104(e1265)* (20),
133 indicating that KIF1A(R11Q), KIF1A(R254Q) and KIF1A(P305L) mutations are loss of function.

134

135 **Synaptic vesicles are mislocalized in homozygotes**

136 UNC-104 is an orthologue of human KIF1A and is a molecular motor that determines the
137 localization of synaptic vesicles in *C. elegans*; therefore, we visualized synaptic vesicles in KAND
138 model worms. The DA9 neuron in *C. elegans* is highly polarized and forms *en passant* synapses
139 along the dorsal side of the axon (32) (Figure 2A). The characteristic morphology of DA9 is suitable
140 for analyzing axonal transport and synaptic localization (33). We expressed a synaptic vesicle
141 marker GFP::*RAB-3* in the DA9 neuron using the *itr-1* promoter to visualize DA9 synapses (Figure
142 2B). In KAND models, GFP::*RAB-3* signals were reduced in the axon and misaccumulated in the
143 dendrite (Figure 2C–F). Only a trace amount of GFP::*RAB-3* signal was observed in the DA9 axon
144 in KAND models.

145 We then observed axonal transport of synaptic vesicle precursors in the proximal region of the DA9
146 axon (33) (Figure 2A, magenta circle). We used GFP::RAB-3 as a representative marker for axonal
147 transport of synaptic vesicle precursors because previous studies have shown that GFP::RAB-3
148 co-migrates with other synaptic vesicle and pre-synaptic proteins in the axon and is, therefore, a
149 good marker to visualize axonal transport (6, 19, 33). In the wild-type worms, both anterograde and
150 retrograde transport were observed in the axon (Figure 2G and H). In contrast, the frequency of both
151 anterograde and retrograde events was significantly reduced in all three mutant strains (Figure 2G
152 and H). In more than 70% of mutant worms, no vesicular movement was detected in the 30 sec time
153 window. These data indicate that axonal transport of synaptic vesicles is strongly affected in
154 *unc-104(R9Q)*, *unc-104(R251Q)* and *unc-104(P298L)* strains.

155

156 **KAND mutations disrupt the motility of motor proteins *in vitro***

157 To study the effect of KAND mutations *in vitro*, we observed the motility of purified
158 human KIF1A protein using total internal reflection fluorescence (TIRF) microscopy (34, 35). To
159 directly study motility parameters, regulatory domains and cargo binding domains were removed
160 (Figure 3A). The neck coiled-coil domain of mammalian KIF1A does not form stable dimers (36);
161 therefore, we stabilized human KIF1A dimers using a leucine zipper domain as described previously
162 (24, 27). A red fluorescent protein, mScarlet-I, was added to the C-terminus of the protein to observe
163 movement (Figure 3A). Resultant KIF1A homodimers [KIF1A(1–393)::LZ::mSca] were purified by
164 Strep tag and gel filtration (Figure 3B). This recombinant protein was then used to analyze the
165 motility of single KIF1A dimers on microtubules (Figure 3C–J). The motility of
166 KIF1A(1–393)::LZ::mSca dimers was observed at 10 pM (Figure 3C).
167 KIF1A(1–393)(R11Q)::LZ::mSca did not move well on microtubules even at 100 pM (Figure 3D),
168 while KIF1A(1–393)::LZ::mSca was saturated on microtubules under the same conditions (Figure

169 3G). KIF1A(1–393)(R254Q)::LZ::mSca moved on microtubules at 10 pM (Figure 3E). We observed
170 frequent binding of KIF1A(1–393)(R254Q)::LZ::mSca with microtubules (Figure 3I) but the
171 velocity was lower and the run length was shorter than for wild type (Figure 3H and J). The landing
172 rate of KIF1A(1–393)(P305L)::LZ::mSca was significantly lower than wild type (Figure 3I),
173 consistent with previous studies (24, 27). Although affected parameters were different depending on
174 the mutated residues, these data are consistent with the reduced axonal transport phenotypes
175 observed in KAND model worms.

176

177 **Synaptic vesicles are mislocalized in heterozygous worms**

178 KAND mutations, including KIF1A(R11Q), KIF1A(R254Q) and KIF1A(P305L) studied
179 here, are *de novo* and cause neuropathies in an autosomal dominant manner. Moreover, KAND is a
180 progressive disease. We therefore analyzed neuronal phenotypes of heterozygous worms in late adult
181 stages (Figure 4A–F). DA9 synapses were analyzed in heterozygotes at 3 and 6 days after the final
182 molt. The morphology of wild-type synapses was mostly maintained in 3 and 6-day-old adults
183 (Figure 4A, C and E). More than 70% of wild-type worms did not show misaccumulation of
184 GFP::RAB-3 in the proximal axon and dendrite at 3 and 6 days. However, 45 to 70% of
185 *unc-104(R9Q)/+*, *unc-104(R251Q)/+* and *unc-104(P298L)/+* animals showed misaccumulation of
186 GFP::RAB-3 in the proximal axon or dendrite (Figure 4B, D and E). To analyze the movement of
187 heterozygous worms, the number of body bends in a water drop was counted for one minute at day 3,
188 6 and 9 (Figure 4F). The motility defects were not strong but there was a tendency for heterozygous
189 worms to show reduced motility compared with wild-type worms.

190

191 **Reduced Axonal transport in heterozygous worms**

192 The DA9 axon and dendrite have plus-end out and minus-end out microtubules, respectively (37).

193 Thus, the mislocalization of synaptic vesicles in the proximal axon and dendrite indicate that
194 anterograde transport is reduced in *unc-104(R9Q)/+*, *unc-104(R251Q)/+* and *unc-104(P298L)/+*
195 worms. We therefore analyzed axonal transport of synaptic vesicle precursors visualized using
196 GFP::*RAB-3* in the DA9 axon as described above (Figure 2A). In *wild type*, *unc-104(R9Q)/+*,
197 *unc-104(R251Q)/+* and *unc-104(P298L)/+* worms, both anterograde and retrograde movement of
198 synaptic vesicle precursors was observed in the DA9 axon (Figure 5A–D). Vesicular movement in
199 heterozygous worms was much better than that in homozygous worms (Figure 2). However, in
200 mutant heterozygotes, the velocity of anterograde axonal transport was reduced. In contrast,
201 retrograde transport, which depends on dynein motors, was not significantly changed in mutant
202 heterozygotes. The frequency of both anterograde and retrograde axonal transport was reduced in
203 mutant heterozygotes compared with that in wild type (Figure 5E–H).

204

205 **Disease mutant/wild type heterodimers have reduced motor properties**

206 The KIF1A motor forms a homodimer for efficient anterograde axonal transport (30). In
207 heterozygotes, half of the motor complex in the neuron is predicted to be heterodimers composed of
208 wild-type KIF1A and disease-associated KIF1A. But the behavior of heterodimers on microtubules
209 remains largely unanalyzed. To analyze the motility of heterodimers at a single-molecule resolution,
210 we purified heterodimers composed of wild-type KIF1A and disease-associated KIF1A. Wild-type
211 KIF1A fused with leucine zipper and mScarlet-I [KIF1A(1–393)::LZ::mSca] and disease-associated
212 KIF1A without fluorescent tag [KIF1A(1–393)::LZ] were co-expressed in bacteria (Figure 6A). The
213 two constructs were respectively fused with a Strep tag and His tag for purification. Tandem affinity
214 purification using His tag and Strep tag followed by gel filtration was performed to purify
215 heterodimers. From a single peak, heterodimers composed of KIF1A(1–393)::LZ::mSca and
216 KIF1A(1–393)::LZ were recovered (Figure 6B). The ratio between the two subunits was calculated

217 from band intensities and the molecular weights were about 1:1, indicating heterodimers.

218 As a positive control, we compared the motility of
219 KIF1A(1–393)::LZ::mSca/KIF1A(1–393)::LZ heterodimers with KIF1A(1–393)::LZ::mSca
220 homodimers (Figure 3C and 6C). Velocity, landing rate and run length of wild-type homodimers and
221 heterodimers were statistically the same (velocity: $1.03 \pm 0.24 \mu\text{m}/\text{sec}$ and $1.03 \pm 0.26 \mu\text{m}/\text{sec}$, run
222 length: $7.99 \pm 6.42 \mu\text{m}$ and $8.07 \pm 6.30 \mu\text{m}$, landing rate: $0.011 \pm 0.003 \mu\text{m}^{-1}\text{s}^{-1}$ and 0.010 ± 0.004
223 $\mu\text{m}^{-1}\text{s}^{-1}$ for homodimers and heterodimers respectively. Mean \pm standard deviation). In contrast,
224 heterodimers composed of wild-type KIF1A and disease-associated KIF1A showed reduced motility
225 (Figure 6C–J). The velocity of KIF1A(1–393)::LZ::mSca/KIF1A(1–393)(R11Q)::LZ,
226 KIF1A(1–393)::LZ::mSca/KIF1A(1–393)(R254Q)::LZ and
227 KIF1A(1–393)::LZ::mSca/KIF1A(1–393)(P305L)::LZ heterodimers was lower than that of
228 wild-type KIF1A (Figure 6H). The landing event of
229 KIF1A(1–393)::LZ::mSca/KIF1A(1–393)(R11Q)::LZ and
230 KIF1A(1–393)::LZ::mSca/KIF1A(1–393)(P305L)::LZ heterodimers on microtubules could not be
231 observed at 10 pM (Figure 6I). At 100 pM, in which wild-type KIF1A homodimers were saturated
232 on microtubules (Figure 6G), the motility of KIF1A(1–393)::LZ::mSca/KIF1A(1–393)(R11Q)::LZ
233 and KIF1A(1–393)::LZ::mSca/KIF1A(1–393)(P305L)::LZ dimers was observed (Figure 6D, F and
234 I) but the run lengths of these wild-type/mutant dimers were much shorter compared with that of
235 wild-type dimers (Figure 6J). The landing rate of
236 KIF1A(1–393)::LZ::mSca/KIF1A(1–393)(R254Q)::LZ heterodimers was higher than that of
237 wild-type dimers (Figure 6I). However, run length of
238 KIF1A(1–393)LZ-mSca/KIF1A(1–393)(R254Q)LZ heterodimers was shorter than that of wild-type
239 dimers (Figure 6J). These results show that KAND mutations strongly affect the landing rate and
240 motility parameters in heterodimers with wild-type KIF1A.

241 Finally, to show that a KAND mutation dominant negatively inhibits axonal transport *in*
242 *vivo*, an *unc-104(R9Q)* cDNA corresponding to the KIF1A(R11Q) mutant, was overexpressed in the
243 DA9 neuron (Figure 7A–C). In 70% of UNC-104(R9Q)-overexpressed animals, synaptic vesicles
244 misaccumulated in the proximal region of the DA9 axon (Figure 7B and C). This phenotype is
245 similar to a weak loss-of-function allele of *unc-104* (38), indicating that KAND mutations inhibit
246 axonal transport by counteracting wild-type motor activity.

247

248 **Discussion**

249 Axonal transport motors form homodimers that move processively on microtubules (39).
250 When a mutation in a motor protein gene is dominant, and if the mutation does not affect the
251 stability or expression of the protein, half of the motor dimers in the cell are predicted to be
252 heterodimers composed of wild-type motor and disease-associated motor. Many disease-associated
253 mutations in motor proteins are caused by autosomal dominant mutations; however, little attention
254 has been paid to the properties of heterodimers in motor-associated diseases. Previous studies have
255 mainly analyzed properties of disease-associated homodimers but not heterodimers (23, 24, 40, 41).
256 We show here that disease-associated KIF1A perturbs the function of wild-type KIF1A by forming
257 dimers. Interestingly, properties of wild-type/mutant heterodimers are different from those of
258 wild-type homodimers and mutant homodimers (Figure 3 and 6). Even though KIF1A(R11Q)
259 homodimers do not show any processive movement, KIF1A(R11Q)/KIF1A(WT) heterodimers
260 showed processive motility (Fig 3D and 6D). These suggest an importance of analyzing the
261 properties of heterodimers. A previous study has analyzed the effect of heterodimerization in a
262 semi-*in vitro* reconstitution in which motor proteins in COS-7 cell lysates, but not purified motor
263 proteins, are observed (29). Some important phenomena, such as landing motor proteins on
264 microtubules, cannot be quantitatively analyzed in the semi-*in vitro* reconstitution system because it

265 is difficult to precisely control the concentration of motors. In our study, using purified heterodimers,
266 we demonstrate that the landing rate of KIF1A(wt)/KIF1A(R11Q) and KIF1A(wt)/KIF1A(P305L) is
267 significantly lower than that of wild-type KIF1A. As KIF1A(R11Q) and KIF1A(P305L)
268 homodimers also have a much lower landing rate than wild-type KIF1A, these mutant subunits
269 inhibit the landing rate of wild-type subunits. KIF1A(R254Q) has a high landing rate and therefore
270 inhibits wild-type KIF1A by a different mechanism, as described below. Mutations in other axonal
271 transport motors, such as KIF5A and cytoplasmic dynein heavy chain 1 genes, are causes of
272 autosomal dominant neuropathies (40-42). Similar phenomena to those observed here may underlie
273 the pathogenesis of these neuropathies and it would be interesting to analyze heterodimers composed
274 of wild-type and disease-associated motors in these cases. In the axon, multiple motors bind to and
275 cooperatively transport a vesicle (43). Disease-associated KIF5A homodimers, which have lower
276 motor activity than wild-type homodimers, inhibit the activity of wild-type KIF5A homodimers
277 when mixed in the microtubule-gliding assay, which mimics cooperative transport (44). Considering
278 this, both mutant KIF1A homodimers and wild-type/mutant KIF1A heterodimers, which both have
279 lower motor activities (Figure 3 and 6), should dominant negatively perturb wild-type homodimers
280 and axonal transport of cargo vesicles (Figure 7D). Consistent with this idea, overexpression of
281 UNC-104(R9Q), mimicking KIF1A(R11Q), causes mislocalization of synaptic vesicles in wild-type
282 neurons (Figure 7A–C). Reconstitution using a chassis composed of recombinant kinesins and DNA
283 origami would help quantify how mutant homodimers and wild-type/mutant heterodimers inhibit
284 axonal transport in KAND (45, 46).

285 Our worm models and single molecule analyses indicate that the velocity of axonal
286 transport is affected by *de novo* autosomal dominant KAND mutations. The frequency of vesicle
287 transport is reduced in disease worm models. Previous studies have suggested that the landing rate of
288 KIF1A is a significant parameter in the pathogenesis of KAND (22, 27). KIF1A(V8M) and

289 KIF1A(P305L) are gain of function and loss of function mutants with elevated and reduced landing
290 rate, respectively. Our result of KIF1A(R11Q) having a significantly lower landing rate is consistent
291 with these findings. Model worms expressing KIF1A(R11Q) showed reduced axonal transport. In
292 contrast, KIF1A(R254Q) showed an elevated landing rate but its velocity and run length were
293 reduced. A previous study has shown that KIF1A dimers are faster than and have a much longer run
294 length than another axonal transporter, KIF5 (47). Interestingly, the velocity of KIF1A(R254Q)
295 shown here is comparable to that of KIF5 and the run length of KIF1A(R254Q) is still longer than
296 that of KIF5. It is possible that the high velocity and/or the extremely long run length of KIF1A is
297 fundamental to axonal transport of synaptic vesicle precursors, although the involvement of other
298 parameters has not been completely excluded.

299 While homozygous disease model worms show strong synaptic phenotypes, heterozygous
300 model worms have clear but mild phenotypes (Figures 1 and 4). In the case of human, autosomal
301 dominant KAND mutations cause severe neuropathies. These differences would arise from the fact
302 that human has complicated neuronal networks and highly developed brain functions. Nevertheless,
303 we think our worm model is useful. Currently, there is no good strategy for KAND treatment. *C.*
304 *elegans* is a powerful tool to perform suppressor screening. We suggest that the worm models
305 established here can be a foundation for genetic and drug screening to search for therapies to treat
306 KAND.

307

308 **Methods**

309 ***Worm experiments***

310 *C. elegans* strains were maintained as described previously (48). N2 wild-type worms and OP50
311 feeder bacteria were obtained from the *C. elegans* genetic center (CGC)(Minneapolis, MN, USA).
312 Nematode growth medium agar plates were prepared as described (48). Transformation of *C.*

313 *elegans* was performed by DNA injection as described (49). The swim test was performed as
314 described previously (50).

315

316 **Genome editing**

317 Target sequences for cas9 and repair templates used to make *unc-104* mutants are described in
318 **supplementary table S1**. Target sequences were inserted into pRB1017 (a gift from Andrew Fire,
319 Stanford University, addgene #59936). pDD162 (a gift from Bob Goldstein, UNC Chapel Hill,
320 addgene #47549) was used to express Cas9. These vectors and oligonucleotides were injected into
321 young adult worms as described with a slight modification (31). For *unc-104(R251Q)*, 50 ng of
322 PDD162, 50 ng of *unc-104(A252V)#4* and 0.6 μ M of repair template were mixed and injected.
323 Worms with a strong *unc* phenotype in the next generation were directly picked and genotyped by
324 PCR. For *unc-104(R9Q)* and *unc-104(P298L)*, 50 ng of pDD162, 50 ng of sgRNA expression
325 plasmid for *unc-104*, 50 ng of sgRNA expression plasmid for *ben-1*, and 0.6 μ M of repair template
326 for *unc-104* were mixed and injected. Injected worms were put on nematode growth medium plates
327 with OP50 feeder bacteria supplemented with 10 μ g/ml benzoimidazole. The next generation was
328 scored and benzoimidazole-resistant worms were picked and genotyped by PCR.

329

330 **Strains**

331 Strains used in this study are described in **supplementary table S2**. Male worms carrying *wyIs85* and
332 *wyIs251* were generated by a heat shock procedure. Heterozygotes were generated by crossing
333 *unc-104* homozygotes with *wyIs85* or *wyIs251* males. Homozygotes show strong *unc* phenotypes,
334 while heterozygotes do not. F1 worms showing non-*unc* phenotypes at the L4 stage were picked and
335 transferred to new plates.

336

337 ***Statistical analyses and graph preparation***

338 Statistical analyses were performed using Graph Pad Prism version 9. Statistical methods are
339 described in the figure legends. Graphs were prepared using Graph Pad Prism version 9, exported in
340 the TIFF format and aligned by Adobe Illustrator 2021.

341

342 ***Purification of homodimers***

343 Reagents were purchased from Nacalai tesque (Kyoto, Japan), unless described. Plasmids to express
344 recombinant KIF1A are described in *supplementary table S3*. To purify
345 KIF1A(1–393)::LZ::mScarlet-I::Strep homodimers, BL21(DE3) was transformed and selected on
346 LB agar supplemented with kanamycin at 37°C overnight. Colonies were picked and cultured in 10
347 ml LB medium supplemented with kanamycin overnight. Next morning, 5 ml of the medium was
348 transferred to 500 ml 2.5× YT (20 g/L Tryptone, 12.5 g/L Yeast Extract, 6.5 g/L NaCl) supplemented
349 with 10 mM phosphate buffer (pH 7.4) and 50 µg/ml kanamycin in a 2 L flask and shaken at 37°C.
350 Two flasks were routinely prepared. When OD₆₀₀ reached 0.6, flasks were cooled in ice-cold water
351 for 30 min. Then, 23.8 mg IPTG was added to each flask. Final concentration of IPTG was 0.2 mM.
352 Flasks were shaken at 18°C overnight.

353 Next day, bacteria expressing recombinant proteins were pelleted by centrifugation (3000 g, 10 min,
354 4°C), resuspended in PBS and centrifuged again (3000 g, 10 min, 4°C). Pellets were resuspended in
355 protein buffer (50 mM Hepes, pH 8.0, 150 mM KCH₃COO, 2 mM MgSO₄, 1 mM EGTA, 10%
356 glycerol) supplemented with Phenylmethylsulfonyl fluoride (PMSF). Bacteria were lysed using a
357 French Press G-M (Glen Mills, NJ, USA) as described by the manufacturer. Lysate was obtained by
358 centrifugation (75,000 g, 20 min, 4°C). Lysate was loaded on Streptactin-XT resin (IBA Lifesciences,
359 Göttingen, Germany) (bead volume: 2 ml). The resin was washed with 40 ml Strep wash buffer (50
360 mM Hepes, pH 8.0, 450 mM KCH₃COO, 2 mM MgSO₄, 1 mM EGTA, 10% glycerol). Protein was

361 eluted with 40 ml Strep elution buffer (50 mM Hepes, pH 8.0, 150 mM KCH₃COO, 2 mM MgSO₄, 1
362 mM EGTA, 10% glycerol, 300 mM biotin). Eluted solution was concentrated using an Amicon Ultra
363 15 (Merck) and then separated on an NGC chromatography system (Bio-Rad) equipped with a
364 Superdex 200 Increase 10/300 GL column (Cytiva). Peak fractions were collected and concentrated
365 using an Amicon Ultra 4 (Merck). Concentrated proteins were aliquoted and snap frozen in liquid
366 nitrogen.

367

368 ***Purification of heterodimers***

369 BL21(DE3) cells transformed with KIF1A(1–393)::LZ::mScarlet-I::Strep plasmid were cultured in
370 LB supplemented with kanamycin at 37°C. Competent cells were prepared using a Mix&Go kit
371 (Zymogen). The competent cells were further transformed with KIF1A(1–393)::LZ::His plasmid and
372 selected on LB agar supplemented with ampicillin and kanamycin. Colonies were picked and
373 cultured in 10 ml LB medium supplemented with ampicillin and kanamycin overnight. Next
374 morning, 5 ml of the medium was transferred to 500 ml 2.5× YT supplemented with carbenicillin
375 and kanamycin in a 2 L flask and shaken at 37°C. Two flasks were routinely prepared. The
376 procedures for protein expression in bacteria and preparation of bacterial lysate were the same as for
377 the purification of homodimers. Lysate was loaded on Streptactin-XT resin (bead volume: 2 ml). The
378 resin was washed with 40 ml wash buffer. Protein was eluted with 40 ml protein buffer
379 supplemented with 300 mM biotin. Eluted solution was then loaded on TALON resin (Takara Bio
380 Inc., Kusatsu, Japan)(bead volume: 2 ml). The resin was washed with 40 ml His-tag wash buffer (50
381 mM Hepes, pH 8.0, 450 mM KCH₃COO, 2 mM MgSO₄, 10 mM imidazole, 10% glycerol) and
382 eluted with His-tag elution buffer (50 mM Hepes, pH 8.0, 450 mM KCH₃COO, 2 mM MgSO₄, 10%
383 glycerol, 500 mM imidazole). Eluted solution was concentrated using an Amicon Ultra 15 and then
384 separated on an NGC chromatography system (Bio-Rad) equipped with a Superdex 200 Increase

385 10/300 GL column (Cytiva). Peak fractions were collected and concentrated using an Amicon Ultra
386 4. Concentrated proteins were aliquoted and snap frozen in liquid nitrogen.

387

388 ***TIRF single-molecule motility assays***

389 TIRF assays were performed as described (22). Tubulin was purified from porcine brain as described
390 (51). Tubulin was labeled with Biotin-PEG₂-NHS ester (Tokyo Chemical Industry, Tokyo, Japan)
391 and AZDye647 NHS ester (Fluoroprobes, Scottsdale, AZ, USA) as described (52). To polymerize
392 Taxol-stabilized microtubules labeled with biotin and AZDye647, 30 μ M unlabeled tubulin, 1.5 μ M
393 biotin-labeled tubulin and 1.5 μ M AZDye647-labeled tubulin were mixed in BRB80 buffer
394 supplemented with 1 mM GTP and incubated for 15 min at 37°C. Then, an equal amount of BRB80
395 supplemented with 40 μ M taxol was added and further incubated for more than 15 min. The solution
396 was loaded on BRB80 supplemented with 300 mM sucrose and 20 μ M taxol and ultracentrifuged at
397 100,000 g for 5 min at 30°C. The pellet was resuspended in BRB80 supplemented with 20 μ M taxol.
398 Glass chambers were prepared by acid washing as previously described (35). Polymerized
399 microtubules were flowed into streptavidin adsorbed flow chambers and allowed to adhere for 5–10
400 min. Unbound microtubules were washed away using assay buffer [30 mM Hepes pH 7.4, 50 mM
401 KCH₃COO, 2 mM Mg(CH₃COO)₂, 1 mM EGTA, 10% glycerol, 0.1 mg/ml biotin-BSA, 0.2 mg/ml
402 kappa-casein, 0.5% Pluronic F127, 1 mM ATP, and an oxygen scavenging system composed of
403 PCA/PCD/Trolox. Purified motor protein was diluted to indicated concentrations in the assay buffer.
404 Then, the solution was flowed into the glass chamber. An ECLIPSE Ti2-E microscope equipped with
405 a CFI Apochromat TIRF 100XC Oil objective lens, an Andor iXion life 897 camera and a Ti2-LAPP
406 illumination system (Nikon, Tokyo, Japan) was used to observe single molecule motility.
407 NIS-Elements AR software ver. 5.2 (Nikon) was used to control the system.

408

409 **Data Availability**

410 All study data are included in the article and/or supporting information.

411

412 **Competing interest**

413 The authors declare no competing interest.

414

415 **Author contribution**

416 S.N. designed research; Y.A., T.K and S.N. performed research; Y.A., T.K and S.N. analyzed data;

417 Y.A., T.K., K.H. and S.N. wrote the paper.

418

419 **Acknowledgements**

420 YA was supported by the Advanced Graduate Program for Future Medicine and Health Care, Tohoku
421 University. KH was supported by JST PRESTO (grant No. JPMJPR1877) and FRIS Creative
422 Interdisciplinary Research Program, Tohoku University. SN was supported by JSPS KAKENHI
423 (20H03247, 19H04738, 20K21378), the Naito foundation and the Uehara foundation. Some worm
424 strains and OP50 were obtained from the CGC. We thank Jeremy Allen, PhD, from Edanz
425 (<https://jp.edanz.com/ac>) for editing a draft of this manuscript.

426

427 **References**

- 428 1. S. Ochs, Fast transport of materials in mammalian nerve fibers. *Science* **176**, 252-260 (1972).
- 429 2. E. L. Holzbaur, S. S. Scherer, Microtubules, axonal transport, and neuropathy. *N Engl J Med* **365**,
430 2330-2332 (2011).
- 431 3. N. Hirokawa, Y. Noda, Y. Tanaka, S. Niwa, Kinesin superfamily motor proteins and intracellular
432 transport. *Nat Rev Mol Cell Biol* **10**, 682-696 (2009).
- 433 4. J. E. Heuser, T. S. Reese, Evidence for recycling of synaptic vesicle membrane during
434 transmitter release at the frog neuromuscular junction. *J Cell Biol* **57**, 315-344 (1973).
- 435 5. Y. Okada, H. Yamazaki, Y. Sekine-Aizawa, N. Hirokawa, The neuron-specific kinesin

- 436 superfamily protein KIF1A is a unique monomeric motor for anterograde axonal transport of
437 synaptic vesicle precursors. *Cell* **81**, 769-780 (1995).
- 438 6. S. Niwa, Y. Tanaka, N. Hirokawa, KIF1Bbeta- and KIF1A-mediated axonal transport of
439 presynaptic regulator Rab3 occurs in a GTP-dependent manner through DENN/MADD. *Nat Cell*
440 *Biol* **10**, 1269-1279 (2008).
- 441 7. M. Kikkawa *et al.*, Switch-based mechanism of kinesin motors. *Nature* **411**, 439-445 (2001).
- 442 8. R. Nitta, M. Kikkawa, Y. Okada, N. Hirokawa, KIF1A alternately uses two loops to bind
443 microtubules. *Science* **305**, 678-683 (2004).
- 444 9. O. I. Wagner *et al.*, Synaptic scaffolding protein SYD-2 clusters and activates kinesin-3
445 UNC-104 in *C. elegans*. *Proc Natl Acad Sci U S A* **106**, 19605-19610 (2009).
- 446 10. D. R. Klopfenstein, R. D. Vale, The lipid binding pleckstrin homology domain in UNC-104
447 kinesin is necessary for synaptic vesicle transport in *Caenorhabditis elegans*. *Molecular Biology*
448 *of the Cell* **15**, 3729-3739 (2004).
- 449 11. R. Stucchi *et al.*, Regulation of KIF1A-Driven Dense Core Vesicle Transport: Ca(2+)/CaM
450 Controls DCV Binding and Liprin-alpha/TANC2 Recruits DCVs to Postsynaptic Sites. *Cell Rep*
451 **24**, 685-700 (2018).
- 452 12. D. T. Byrd *et al.*, UNC-16, a JNK-signaling scaffold protein, regulates vesicle transport in *C.*
453 *elegans*. *Neuron* **32**, 787-800 (2001).
- 454 13. Q. Zheng *et al.*, The vesicle protein SAM-4 regulates the processivity of synaptic vesicle
455 transport. *PLoS Genet* **10**, e1004644 (2014).
- 456 14. S. Yogev, R. Cooper, R. Fetter, M. Horowitz, K. Shen, Microtubule Organization Determines
457 Axonal Transport Dynamics. *Neuron* **92**, 449-460 (2016).
- 458 15. M. P. Klassen *et al.*, An Arf-like small G protein, ARL-8, promotes the axonal transport of
459 presynaptic cargoes by suppressing vesicle aggregation. *Neuron* **66**, 710-723 (2010).
- 460 16. S. P. Koushika *et al.*, Mutations in *Caenorhabditis elegans* cytoplasmic dynein components
461 reveal specificity of neuronal retrograde cargo. *J Neurosci* **24**, 3907-3916 (2004).
- 462 17. J. Kumar *et al.*, The *Caenorhabditis elegans* Kinesin-3 motor UNC-104/KIF1A is degraded upon
463 loss of specific binding to cargo. *PLoS Genet* **6**, e1001200 (2010).
- 464 18. S. Niwa *et al.*, Autoinhibition of a Neuronal Kinesin UNC-104/KIF1A Regulates the Size and
465 Density of Synapses. *Cell Rep* **16**, 2129-2141 (2016).
- 466 19. S. Niwa *et al.*, BORC Regulates the Axonal Transport of Synaptic Vesicle Precursors by
467 Activating ARL-8. *Curr Biol* **27**, 2569-2578 e2564 (2017).
- 468 20. D. H. Hall, E. M. Hedgecock, Kinesin-related gene unc-104 is required for axonal transport of
469 synaptic vesicles in *C. elegans*. *Cell* **65**, 837-847 (1991).
- 470 21. A. J. Otsuka *et al.*, The *C. elegans* unc-104 gene encodes a putative kinesin heavy chain-like
471 protein. *Neuron* **6**, 113-122 (1991).

- 472 22. K. Chiba *et al.*, Disease-associated mutations hyperactivate KIF1A motility and anterograde
473 axonal transport of synaptic vesicle precursors. *Proc Natl Acad Sci U S A* **116**, 18429-18434
474 (2019).
- 475 23. S. Esmaeli Nieh *et al.*, De novo mutations in KIF1A cause progressive encephalopathy and
476 brain atrophy. *Ann Clin Transl Neurol* **2**, 623-635 (2015).
- 477 24. L. Boyle *et al.*, Genotype and defects in microtubule-based motility correlate with clinical
478 severity in KIF1A-associated neurological disorder. *HGG Adv* **2** (2021).
- 479 25. T. Nemani *et al.*, KIF1A-related disorders in children: A wide spectrum of central and peripheral
480 nervous system involvement. *J Peripher Nerv Syst* **25**, 117-124 (2020).
- 481 26. C. Ohba *et al.*, De novo KIF1A mutations cause intellectual deficit, cerebellar atrophy, lower
482 limb spasticity and visual disturbance. *J Hum Genet* **60**, 739-742 (2015).
- 483 27. A. J. Lam *et al.*, A highly conserved 310 helix within the kinesin motor domain is critical for
484 kinesin function and human health. *Sci Adv* **7** (2021).
- 485 28. C. Aguilera *et al.*, The Novel KIF1A Missense Variant (R169T) Strongly Reduces Microtubule
486 Stimulated ATPase Activity and Is Associated With NESCAV Syndrome. *Front Neurosci* **15**,
487 618098 (2021).
- 488 29. B. G. Budaitis *et al.*, Pathogenic mutations in the kinesin-3 motor KIF1A diminish force
489 generation and movement through allosteric mechanisms. *J Cell Biol* **220** (2021).
- 490 30. M. Tomishige, D. R. Klopfenstein, R. D. Vale, Conversion of Unc104/KIF1A kinesin into a
491 processive motor after dimerization. *Science* **297**, 2263-2267 (2002).
- 492 31. J. A. Arribere *et al.*, Efficient marker-free recovery of custom genetic modifications with
493 CRISPR/Cas9 in *Caenorhabditis elegans*. *Genetics* **198**, 837-846 (2014).
- 494 32. M. P. Klassen, K. Shen, Wnt signaling positions neuromuscular connectivity by inhibiting
495 synapse formation in *C. elegans*. *Cell* **130**, 704-716 (2007).
- 496 33. C. I. Maeder, A. San-Miguel, E. Y. Wu, H. Lu, K. Shen, In vivo neuron-wide analysis of synaptic
497 vesicle precursor trafficking. *Traffic* **15**, 273-291 (2014).
- 498 34. R. D. Vale *et al.*, Direct observation of single kinesin molecules moving along microtubules.
499 *Nature* **380**, 451-453 (1996).
- 500 35. R. J. McKenney, W. Huynh, M. E. Tanenbaum, G. Bhabha, R. D. Vale, Activation of cytoplasmic
501 dynein motility by dynactin-cargo adapter complexes. *Science* **345**, 337-341 (2014).
- 502 36. Y. Okada, N. Hirokawa, A processive single-headed motor: kinesin superfamily protein KIF1A.
503 *Science* **283**, 1152-1157 (1999).
- 504 37. J. Yan *et al.*, Kinesin-1 regulates dendrite microtubule polarity in *Caenorhabditis elegans*. *Elife* **2**,
505 e00133 (2013).
- 506 38. L. B. Li *et al.*, The Neuronal Kinesin UNC-104/KIF1A Is a Key Regulator of Synaptic Aging
507 and Insulin Signaling-Regulated Memory. *Curr Biol* **26**, 605-615 (2016).

- 508 39. R. D. Vale, The molecular motor toolbox for intracellular transport. *Cell* **112**, 467-480 (2003).
- 509 40. M. G. Marzo *et al.*, Molecular basis for dyneinopathies reveals insight into dynein regulation and
510 dysfunction. *Elife* **8** (2019).
- 511 41. H. T. Hoang, M. A. Schlager, A. P. Carter, S. L. Bullock, DYNC1H1 mutations associated with
512 neurological diseases compromise processivity of dynein-dynactin-cargo adaptor complexes.
513 *Proc Natl Acad Sci U S A* **114**, E1597-E1606 (2017).
- 514 42. E. Reid *et al.*, A kinesin heavy chain (KIF5A) mutation in hereditary spastic paraplegia (SPG10).
515 *Am J Hum Genet* **71**, 1189-1194 (2002).
- 516 43. K. Hayashi, S. Hasegawa, T. Sagawa, S. Tasaki, S. Niwa, Non-invasive force measurement
517 reveals the number of active kinesins on a synaptic vesicle precursor in axonal transport
518 regulated by ARL-8. *Phys Chem Chem Phys* **20**, 3403-3410 (2018).
- 519 44. B. Ebbing *et al.*, Effect of spastic paraplegia mutations in KIF5A kinesin on transport activity.
520 *Hum Mol Genet* **17**, 1245-1252 (2008).
- 521 45. K. Furuta *et al.*, Measuring collective transport by defined numbers of processive and
522 nonprocessive kinesin motors. *Proc Natl Acad Sci U S A* **110**, 501-506 (2013).
- 523 46. N. D. Derr *et al.*, Tug-of-war in motor protein ensembles revealed with a programmable DNA
524 origami scaffold. *Science* **338**, 662-665 (2012).
- 525 47. V. Soppina *et al.*, Dimerization of mammalian kinesin-3 motors results in superprocessive
526 motion. *Proc Natl Acad Sci U S A* **111**, 5562-5567 (2014).
- 527 48. S. Brenner, The genetics of *Caenorhabditis elegans*. *Genetics* **77**, 71-94 (1974).
- 528 49. C. C. Mello, J. M. Kramer, D. Stinchcomb, V. Ambros, Efficient gene transfer in *C.elegans*:
529 extrachromosomal maintenance and integration of transforming sequences. *EMBO J* **10**,
530 3959-3970 (1991).
- 531 50. J. T. Pierce-Shimomura *et al.*, Genetic analysis of crawling and swimming locomotory patterns
532 in *C. elegans*. *Proc Natl Acad Sci U S A* **105**, 20982-20987 (2008).
- 533 51. M. Castoldi, A. V. Popov, Purification of brain tubulin through two cycles of
534 polymerization-depolymerization in a high-molarity buffer. *Protein Expr Purif* **32**, 83-88 (2003).
- 535 52. J. Al-Bassam, Reconstituting Dynamic Microtubule Polymerization Regulation by TOG Domain
536 Proteins. *Method Enzymol* **540**, 131-148 (2014).

537

538 **Figure legends**

539 **Figure 1 Establishment of disease model worms by genome editing**

540 (A) Schematic drawing of the domain organization of KIF1A motor protein. NC, neck coiled-coil
541 domain. CC1, Coiled-coil 1 domain. FHA, Forkhead-associated domain. CC2, Coiled-coil 2 domain.
542 CC3, Coiled-coil 3 domain. PH, Pleckstrin-homology domain. The three KAND mutations and

543 corresponding *C. elegans* UNC-104 mutations analyzed in this study are indicated.
544 (B) Sequence comparison between human KIF1A and *C. elegans* UNC-104.
545 (C) Macroscopic phenotypes of KAND model homozygotes. Mutant worms are smaller than
546 wild-type worms and do not move well on the bacterial feeder. Bars, 1 mm.
547 (D) Swim test. The number of body bends in a water drop was counted for 1 min and plotted. Dots
548 represents data points. Green bars represent median values. Kruskal-Wallis test followed by Dunn's
549 multiple comparison test. N = 20 worms for each genotype. **, adjusted P value < 0.01. ****,
550 adjusted P value < 0.0001.

551

552 **Figure 2 Synaptic vesicle localization in KAND model homozygous worms**

553 (A) Schematic drawing show the morphology of the DA9 neuron. Green dots along the axon show
554 synaptic vesicle distribution. The magenta circle shows the proximal axon.

555 (B–E) Representative images showing the distribution of synaptic vesicles in the DA9 neuron in *wild*
556 *type* (B), *unc-104(R9Q)* (C), *unc-104(R251Q)* (D), and *unc-104(P298L)* (E). Synaptic vesicles are
557 visualized by GFP::RAB-3. Arrowheads show mislocalization of synaptic vesicles in the dendrite
558 and proximal axon. Bars, 50 μ m.

559 (F) Dot plots showing the number of puncta in the axon (left panel) and dendrite (right panel) of
560 DA9. Ordinary one-way ANOVA followed by Dunnett's multiple comparison test. Green bars show
561 the mean \pm standard deviation (S.D.). N = 60 worms for each genotype. ****, adjusted P value <
562 0.0001.

563 (G) Representative kymographs of *wild type* (upper panel) and *unc-104(R251Q)* (lower panel). The
564 axonal transport of synaptic vesicle precursors was visualized by GFP::RAB-3. The proximal axon
565 shown in panel (A) was observed. Vertical and horizontal bars show 10 seconds and 10 μ m,
566 respectively.

567 (H) Dot plots showing the frequency of anterograde axonal transport (left panel) and retrograde
568 axonal transport (right panel). Green bars represent median values. Kruskal-Wallis test followed by
569 Dunn's multiple comparison test. N = 14 *wild type*, 14 *unc-104(R9Q)*, 18 *unc-104(R251Q)* and 16
570 *unc-104(P298L)* axons. ****, adjusted P Value < 0.0001.

571

572 **Figure 3 Single molecule behavior of disease-associated KIF1A mutants**

573 (A) Schematic drawing of the domain organization of KIF1A motor protein and the recombinant

574 protein analyzed in Figure 3.
575 (B) Purified KIF1A(1–393)::LZ::mScarlet and its mutants were separated by SDS-PAGE and
576 detected by trichloroethanol staining. M represents a marker lane. Numbers on the left indicate
577 molecular weight (kDa). Arrow indicates KIF1A(1–393)::LZ::mScarlet.
578 (C–G) Representative kymographs showing the motility of 10 pM KIF1A (wt) (C), 100 pM
579 KIF1A(R11Q) (D), 10 pM KIF1A(R254Q) (E), 100 pM KIF1A(P305L) and 100 pM KIF1A (wt)
580 (G). Vertical and horizontal bars represent 5 sec and 5 μ m, respectively.
581 (H) Dot plots showing the velocity of KIF1A. Each dot indicates one datum. Green bars represent
582 median values. Kruskal-Wallis test followed by Dunn's multiple comparison test. n = 433 (wt), 325
583 (R254Q) and 498 (P305L). *****, adjusted P Value < 0.0001. Note that no processive movement was
584 detected for KIF1A(R11Q).
585 (I) Dot plots showing the landing rate of KIF1A. The number of KIF1A that bound to microtubules
586 was counted and adjusted by the time window and microtubule length. Each dot shows one datum.
587 Green bars represent median values. Kruskal-Wallis test followed by Dunn's multiple comparison
588 test. n = 30 (10 pM wt), 28 (100 pM R11Q), 29 (10 pM R254Q) and 30 (100 pM P305L) movies.
589 *****, adjusted P Value < 0.0001. Note that no landing event was detected in 10 pM KIF1A(R11Q)
590 and KIF1A(P305L) experiments.
591 (J) Dot plots showing the run length of KIF1A. Each dot shows one datum. Green bars represent
592 median values with interquartile ranges. Kruskal-Wallis test followed by Dunn's multiple
593 comparison test. n = 312 (wt), 241 (R254Q) and 243 (P305L) homodimers. *****, adjusted P Value <
594 0.0001.

595

596 **Figure 4 Synaptic vesicle localization of heterozygotes**

597 (A–D) Representative images showing synaptic vesicle distribution in 3 day-day-old *wild-type* adult
598 (A), 3 day-day-old *unc-104(R251Q)/+* adult (B), 6 day-day-old *wild-type* adult (C), and 6
599 day-day-old *unc-104(R251Q)/+* adult (D). Synaptic vesicles are visualized by GFP::RAB-3. Bars,
600 50 μ m.
601 (E) The ratios of worms with dendritic mislocalization of synaptic vesicles to worms showing
602 wild-type localization of synaptic vesicles are shown. Chi-square test adjusted by Bonferroni
603 correction. *, adjusted P Value < 0.05. **, adjusted P Value < 0.01. *****, adjusted P Value < 0.0001.
604 (F) Dot plots showing swim test results at 3, 6 and 9 days-old. Each dot shows one datum. Green

605 bars represent median values. Kruskal-Wallis test followed by Dunn's multiple comparison test. N =
606 34 (wt), 38 (R9Q/+), 32 (R251Q/+) and 35 (P298L/+) (3-day-old adult worms); 36 (wt), 33 (R9Q/+),
607 36 (R251Q/+) and 35 (P298L/+) (6-day-old adult worms); 27 (wt), 30 (R9Q/+), 29 (R251Q/+) and
608 33 (P298L/+) (9-day-old adult worms). ns, adjusted P Value > 0.05 and statistically not significant. *,
609 adjusted P Value < 0.05. **, adjusted P Value < 0.01. ****, adjusted P Value < 0.0001.

610

611 **Figure 5 Axonal transport in KAND model heterozygotes**

612 (A–D) Representative kymographs showing axonal transport of synaptic vesicle precursors in *wild*
613 *type* (A), *unc-104(R9Q)/+* (B), *unc-104(R251Q)/+* (C) and *unc-104(P305L)/+* (D). GFP::RAB-3
614 was used as a marker. Vertical and horizontal bars indicate 10 seconds and 10 μ m, respectively.

615 (E and F) The velocity of axonal transport. The velocity of anterograde transport (E) and retrograde
616 transport (F) are shown as dot plots. (E) Ordinary one-way ANOVA followed by Dunnett's multiple
617 comparison test. Green bars show the mean \pm S.D.. n = 94 (wild-type), 90 (R9Q/+), 66 (R251Q/+)
618 and 117 (P298L/+) vesicles from at least five independent worms. ****, adjusted P Value < 0.0001.

619 (F) Ordinary one-way ANOVA followed by Dunnett's multiple comparison test. Green bars show the
620 mean \pm S.D.. n = 63 (wild-type), 54 (R9Q/+), 38 (R251Q/+) and 53 (P298L/+) vesicles from at least
621 five independent worms. ns, adjusted P Value > 0.05 and no significant statistical difference.

622 (G and H) Frequency of axonal transport. The frequency of anterograde transport (G) and retrograde
623 transport (H) are shown as dot plots. (G) Kruskal-Wallis test followed by Dunn's multiple
624 comparison test. Each dot represents data from each worm. Green bars represent median values. N =
625 14 (wt), 16 (R9Q/+), 18 (R251Q/+) and 19 (P298L/+) independent worms. ****, adjusted P Value <

626 0.0001. (H) Kruskal-Wallis test followed by Dunn's multiple comparison test. Each dot represents
627 data from each worm. Green bars represent median values. N = 14 (wt), 16 (R9Q/+), 18 (R251Q/+)
628 and 19 (P298L/+) independent worms. **, adjusted P Value < 0.01, ****, adjusted P Value < 0.0001.

629

630 **Figure 6 The single molecule behavior of wild type/mutant KIF1A heterodimers**

631 (A) Schematic drawing of the recombinant KIF1A heterodimer analyzed in Figure 6.

632 (B) Purified KIF1A(1–393)::LZ::mScarlet/KIF1A(1–393)::LZ heterodimers were separated by
633 SDS-PAGE and detected by Coomassie brilliant blue staining. M represents marker. Numbers on the
634 left indicate the molecular weight (kDa). Magenta and black arrows indicate
635 KIF1A(1–393)::LZ::mScarlet and KIF1A(1–393)::LZ, respectively.

636 (C–G) Representative kymographs showing the motility of 10 pM KIF1A (wt) (C), 100 pM
637 KIF1A(R11Q) (D), 10 pM KIF1A(R254Q) (E), 100 pM KIF1A(P305L) and 100 pM KIF1A (wt)
638 (G). Vertical and horizontal bars represent 5 sec and 5 μ m, respectively.

639 (H) Dot plots showing the velocity of KIF1A. Each dot shows one datum. Green bars represent
640 median values. Kruskal-Wallis test followed by Dunn's multiple comparison test. n = 308 (wt/wt),
641 315 (wt/R11Q), 294 (wt/R254Q) and 414 (wt/P305L) heterodimers. ****, adjusted P Value <
642 0.0001.

643 (I) Dot plots showing the landing rate of KIF1A. The number of KIF1A molecules that bind to
644 microtubules was counted and adjusted by the time window and microtubule length. Each dot shows
645 one datum. Green bars represent median values. Kruskal-Wallis test followed by Dunn's multiple
646 comparison test. n = 29 (10 pM wt/wt), 29 (100 pM wt/R11Q), 28 (10 pM wt/R254Q) and 38 (100
647 pM wt/P305L) independent observations. **, adjusted P Value < 0.01, ***, adjusted P Value < 0.001,
648 ****, adjusted P Value < 0.0001.

649 (J) Dot plots showing the run length of KIF1A. Each dot shows one datum. Green bars represent
650 median values and interquartile ranges. Kruskal-Wallis test followed by Dunn's multiple comparison
651 test. n = 215 (wt/wt), 241 (wt/R11Q), 195 (wt/R254Q) and 266 (wt/P305L) heterodimers. ****,
652 adjusted P Value < 0.0001.

653

654 **Figure 7 KAND mutations inhibit axonal transport in a dominant negative fashion**

655 (A–C) UNC-104(R9Q) was overexpressed in the *wild-type* background and the localization of
656 synaptic vesicles was observed. (A and B) Representative images showing the localization of
657 synaptic vesicles in *wild-type* (A) and UNC-104(R9Q)-overexpressing worms (B). Arrow heads
658 show synaptic-vesicle accumulated puncta that are mislocalized in the proximal region of the axon.
659 Bars, 50 μ m. (C) Bar graphs showing the ratio of affected animals. Chi-square test. N = 51 (*wt*) and
660 49 [unc-104(R9Q)-overexpressing worm]. ****, p < 0.0001.

661 (D) Schematic drawing showing how vesicular transport is suppressed in KAND patient axons. Not
662 only mutant homodimers but also wild-type/mutant heterodimers inhibit axonal transport of synaptic
663 vesicle precursors.

664

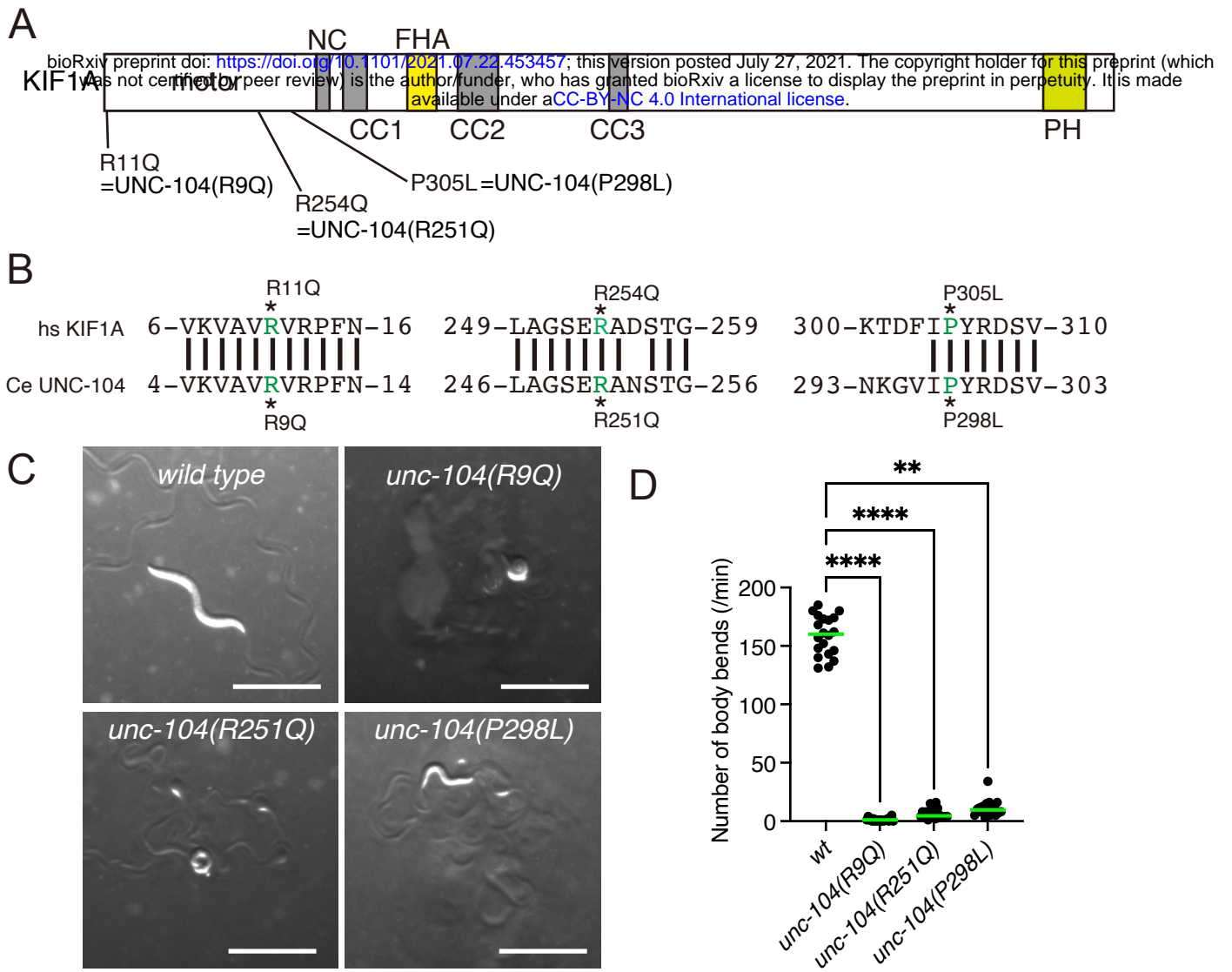


Figure 1

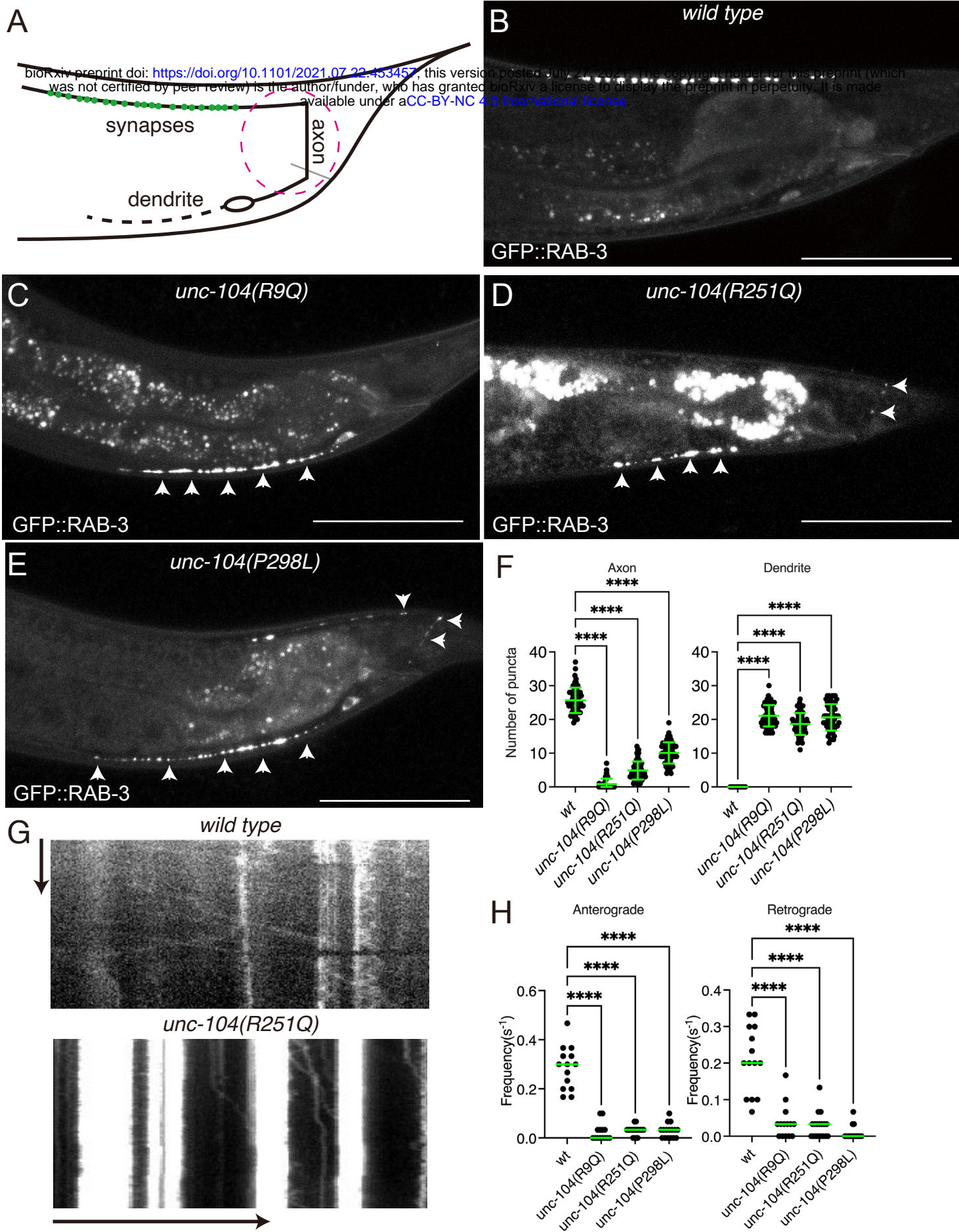


Figure 2

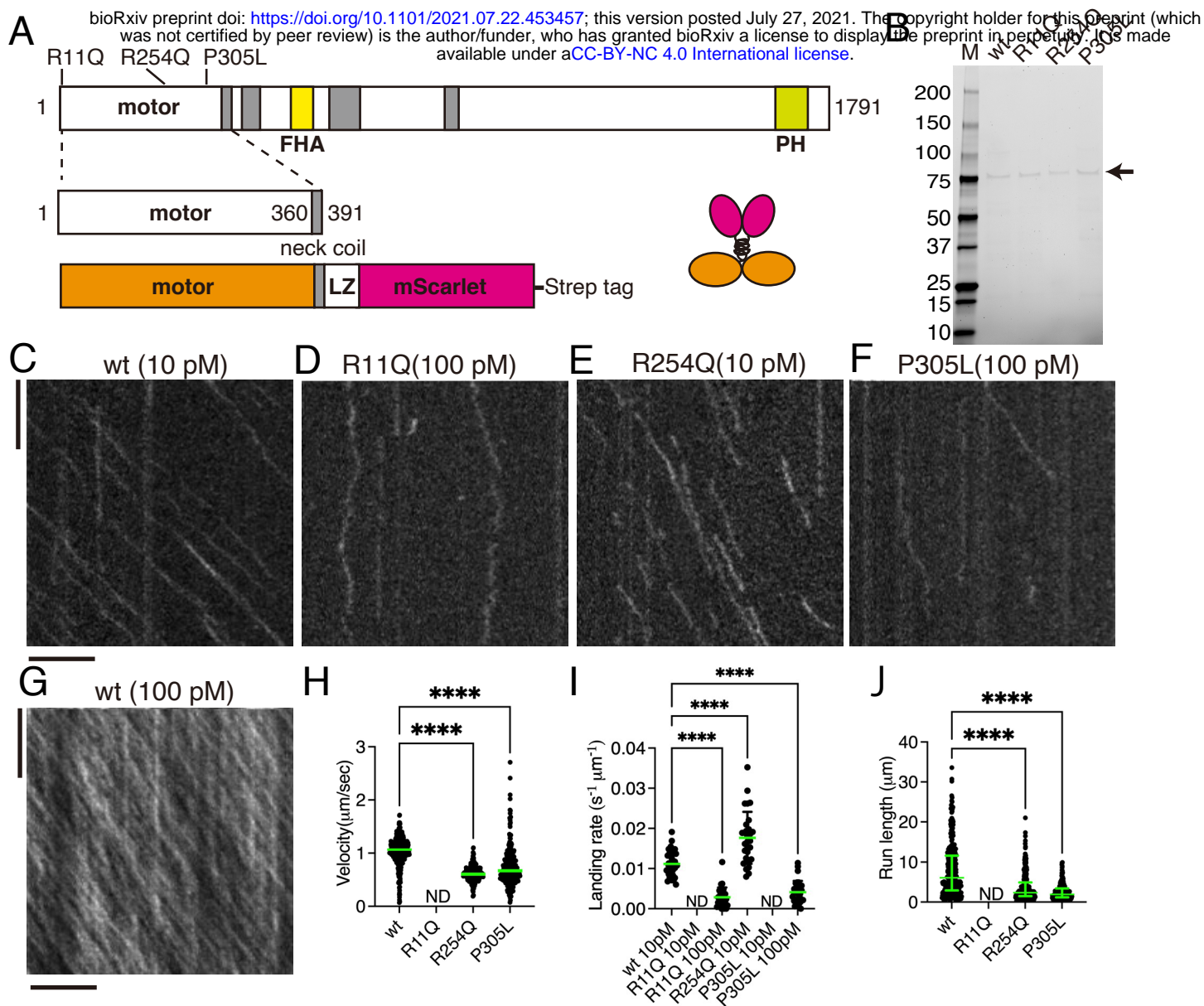


Figure 3

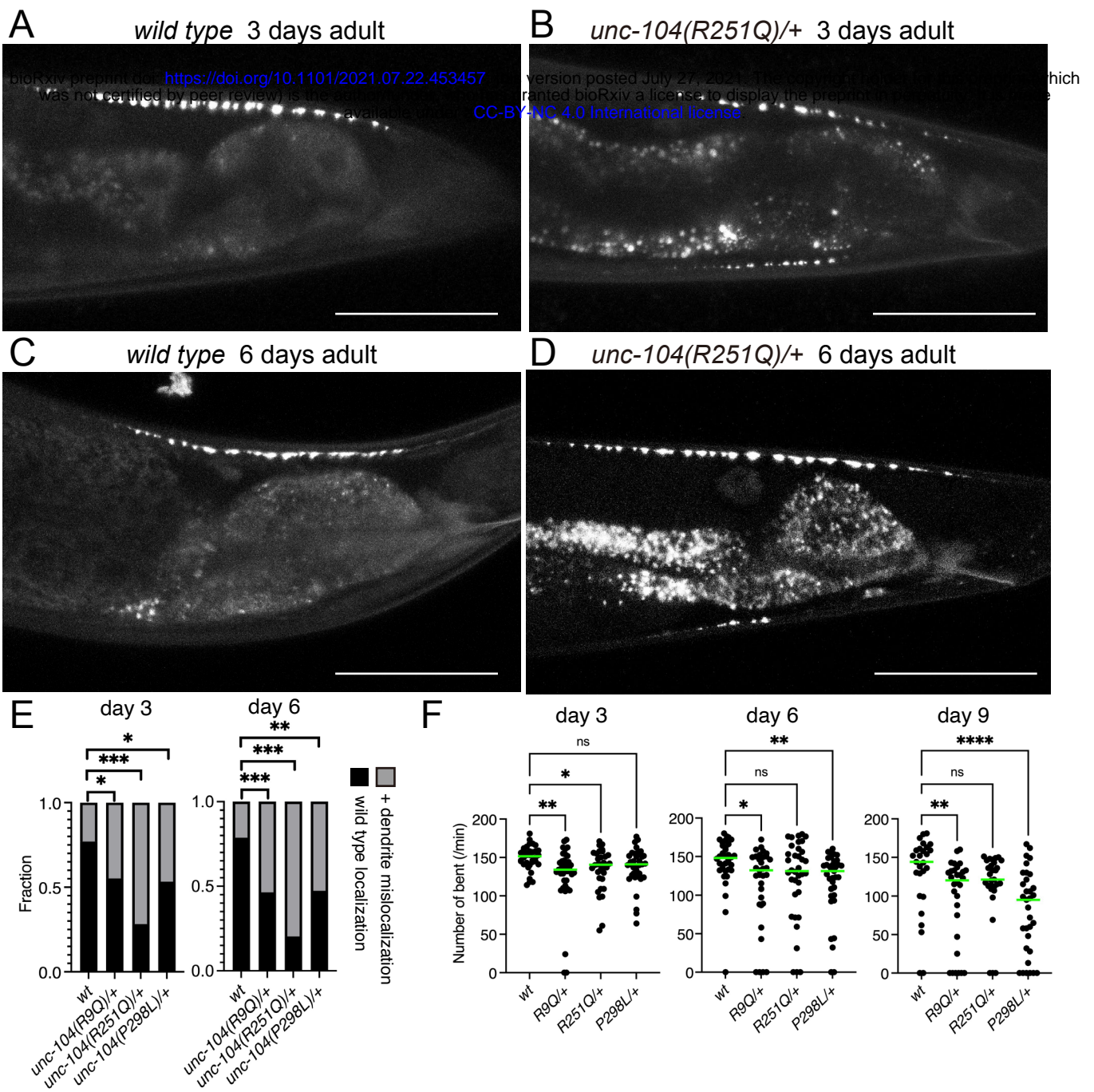


Figure 4

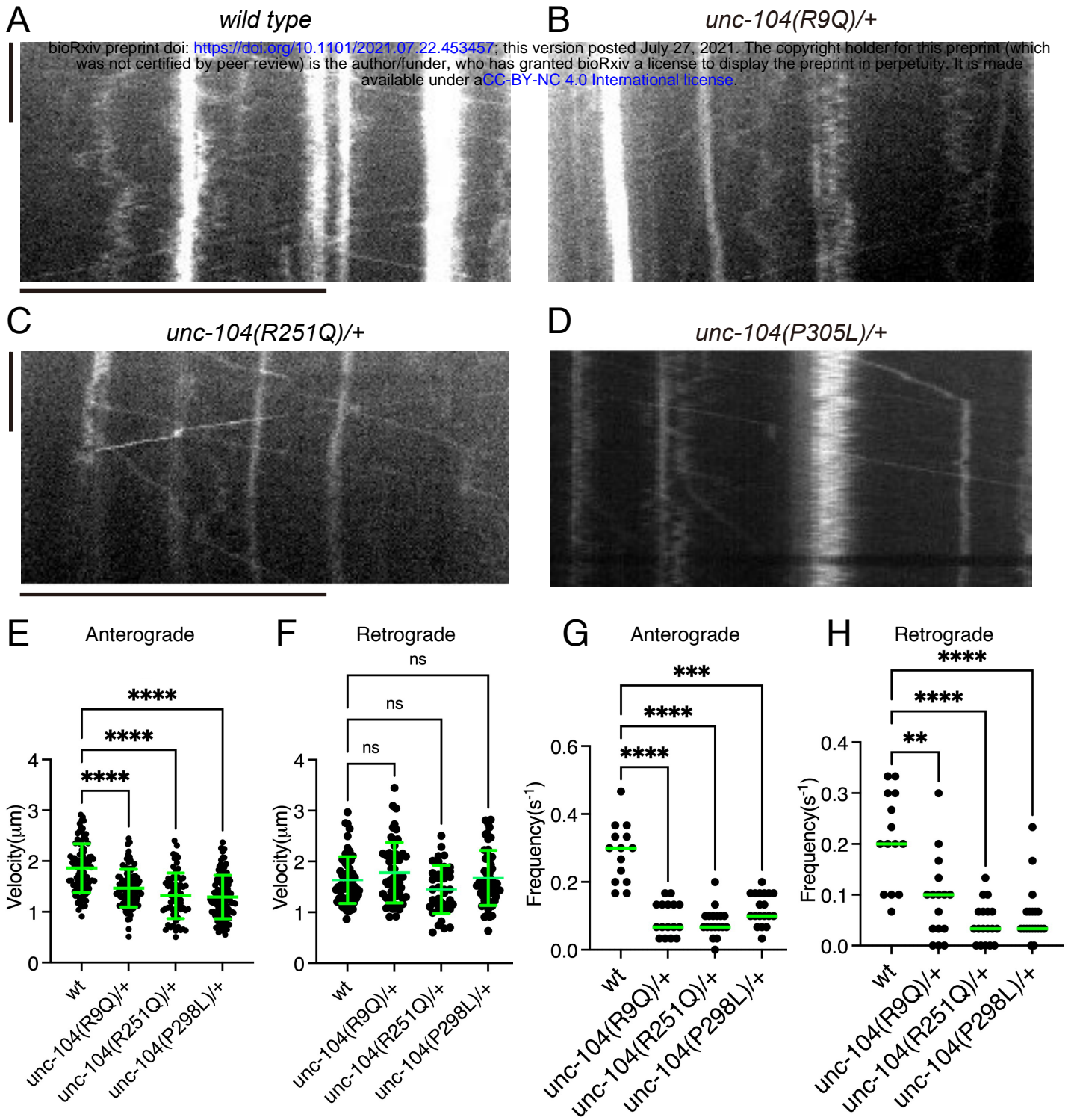
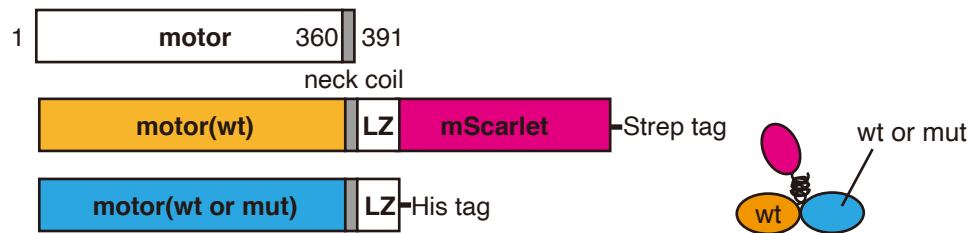


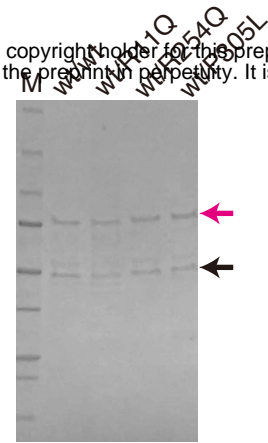
Figure 5

A

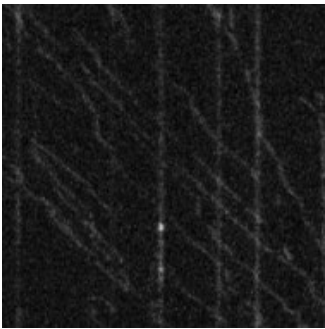
bioRxiv preprint doi: <https://doi.org/10.1101/2021.07.22.453457>; this version posted July 27, 2021. The copyright holder for this preprint (which was not certified by peer review) is the author/funder, who has granted bioRxiv a license to display the preprint in perpetuity. It is made available under aCC-BY-NC 4.0 International license.



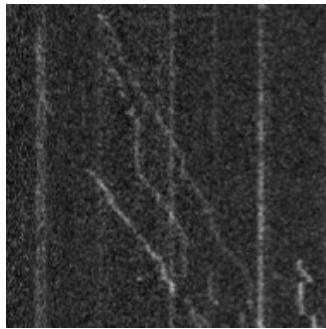
B



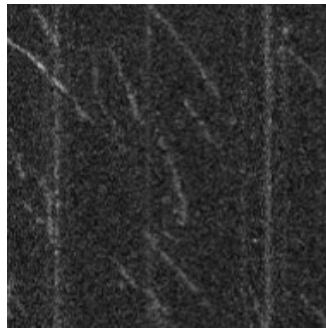
C wt/wt (10 pM)



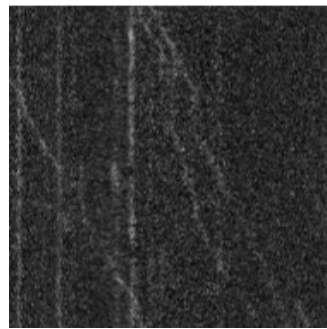
D wt/R11Q(100 pM)



E wt/R254Q(10 pM)



F wt/P305L(100 pM)



G wt/wt (100 pM)

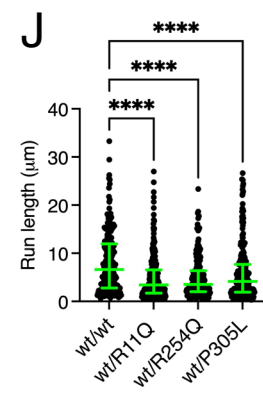
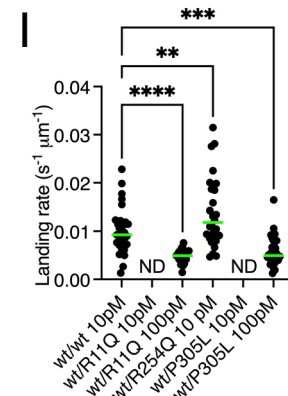
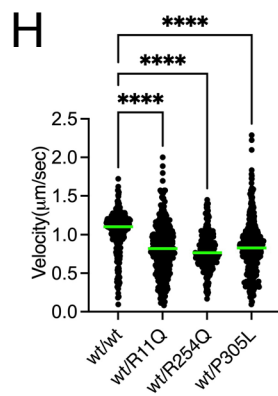
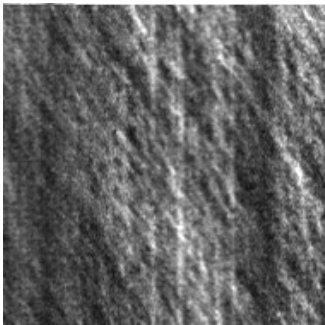


Figure 6

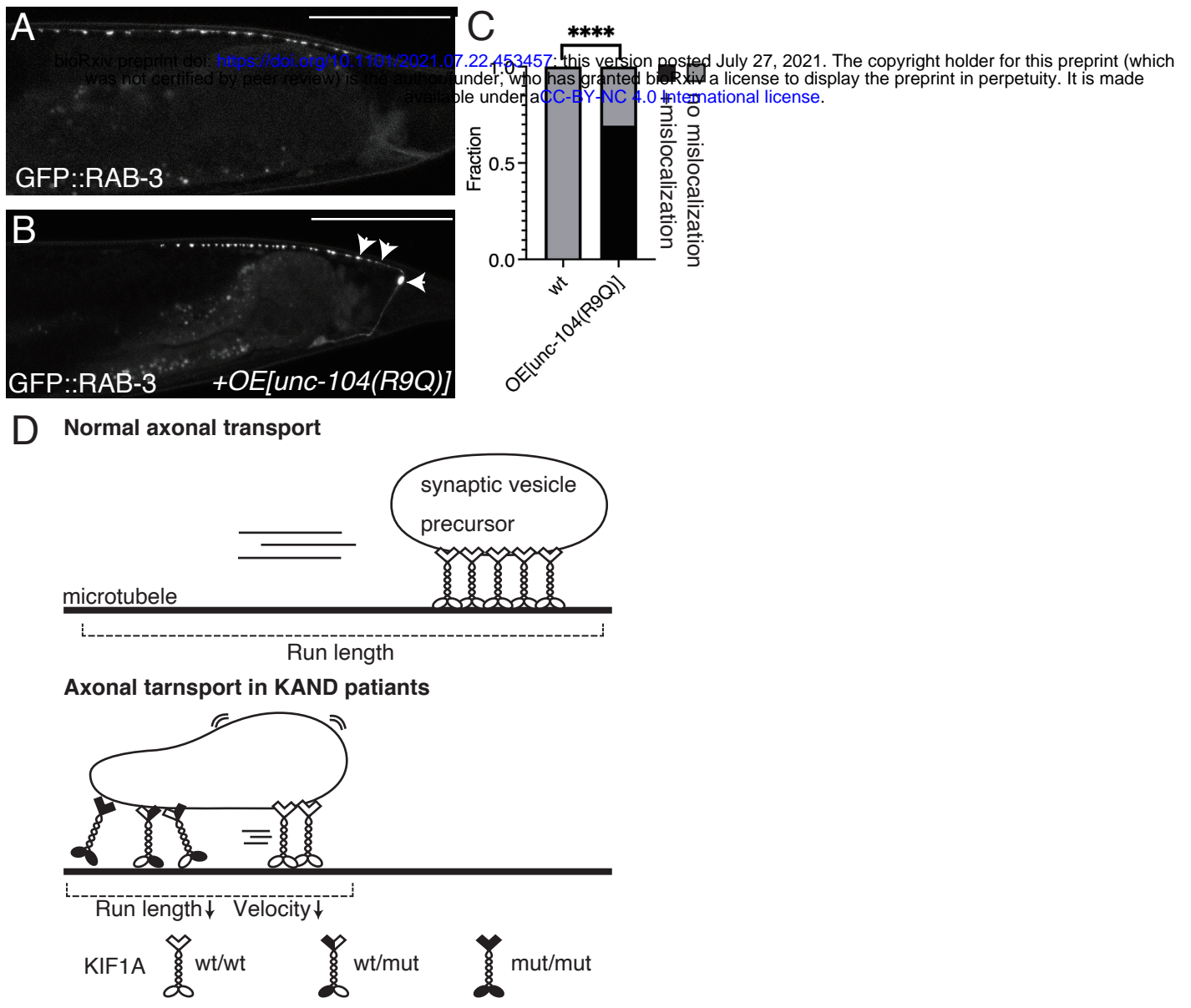


Figure 7